HHS Public Access

Author manuscript

ACS Nano. Author manuscript; available in PMC 2021 January 28.

Published in final edited form as:

ACS Nano. 2020 July 28; 14(7): 8624–8633. doi:10.1021/acsnano.0c03009.

Acoustofluidic Scanning Nanoscope with High Resolution and Large Field of View

Geonsoo Jin,
Department of Mechanical Engineering and Material Science, Duke University, Durham, North Carolina 27708, United States;

Hunter Bachman,
Department of Mechanical Engineering and Material Science, Duke University, Durham, North Carolina 27708, United States;

Ty Downing Naquin,
Department of Mechanical Engineering and Material Science, Duke University, Durham, North Carolina 27708, United States

Joseph Rufo,
Department of Mechanical Engineering and Material Science, Duke University, Durham, North Carolina 27708, United States

Serena Hou,
Department of Mechanical Engineering and Material Science, Duke University, Durham, North Carolina 27708, United States

Zhenhua Tian,
Department of Mechanical Engineering and Material Science, Duke University, Durham, North Carolina 27708, United States

Chenglong Zhao,
Department of Physics and Department of Electro-Optics and Photonics, University of Dayton, Dayton, Ohio 45469, United States;

Tony Jun Huang

Corresponding Authors: **Chenglong Zhao** – Department of Physics and Department of Electro-Optics and Photonics, University of Dayton, Dayton, Ohio 45469, United States; czhao1@udayton.edu, **Tony Jun Huang** – Department of Mechanical Engineering and Material Science, Duke University, Durham, North Carolina 27708, United States; tony.huang@duke.edu.

Supporting Information

The Supporting Information is available free of charge at https://pubs.acs.org/doi/10.1021/acsnano.0c03009.

(Figure S1) magnified images of Blu-ray disc surface are taken by different microscope objective and SEM; (Figures S2) analysis of super-resolution effects in different materials and sizes of microparticles; (Figures S3) simulation results of a 2 μm PS bead along two orthogonal directions with FDTD method; (Figure S4) Ge nanoparticles imaging through a PS-20 microsphere; (Figure S5) schematic explanation of reflection and transmission light illuminations; (Figure S6) comparison of optical resolutions of 800 nm chrome grating patterns of letter “K”; (Table S1) percentage of the FOV imaged versus the number of imaging frames and processing time (PDF)

Movie of microparticles movement by an acoustic energy distribution. (AVI)

Movie of microparticles movement and tracking. (AVI)

Complete contact information is available at: https://pubs.acs.org/10.1021/acsnano.0c03009

The authors declare the following competing financial interest(s): T.J.H. has cofounded a start-up company, Ascent Bio-Nano Technologies Inc., to commercialize technologies involving acoustofluidics and acoustic tweezers.

Department of Mechanical Engineering and Material Science, Duke University, Durham, North Carolina 27708, United States;

Abstract

Optical imaging with nanoscale resolution and a large field of view is highly desirable in many research areas. Unfortunately, it is challenging to achieve these two features simultaneously while using a conventional microscope. An objective lens with a low numerical aperture (NA) has a large field of view but poor resolution. In contrast, a high NA objective lens will have a higher resolution but reduced field of view. In an effort to close the gap between these trade-offs, we introduce an acoustofluidic scanning nanoscope (AS-nanoscope) that can simultaneously achieve high resolution with a large field of view. The AS-nanoscope relies on acoustofluidic-assisted scanning of multiple microsized particles. A scanned 2D image is then compiled by processing the microparticle images using an automated big-data image algorithm. The AS-nanoscope has the potential to be integrated into a conventional microscope or could serve as a stand-alone instrument for a wide range of applications where both high resolution and large field of view are required.

Graphical Abstract

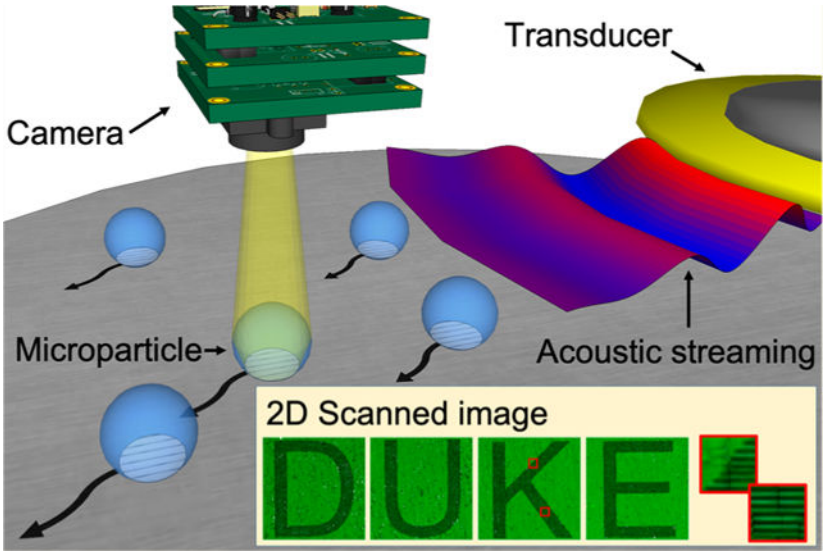

Keywords

scanning nanoscope; acoustic streaming; super resolution; image processing; acoustofluidics

The optical microscope, invented centuries ago, is a ubiquitous tool in many industrial and research settings due to its rapid and noninvasive imaging capability[1,2] compared to higher-resolution imaging instruments, such as scanning electron microscopes (SEMs),[3,4] atomic force microscopes (AFMs),[5] and transmission electron microscopes (TEMs).[6] A key element in a conventional optical microscope is the objective lens, which plays the most important role in determining the resolving power of the imaging system and is generally

expensive because of the complex stacks of lenses needed to correct various image aberrations. Despite its widespread usage in different fields, a conventional optical microscope lacks the ability to simultaneously realize high-resolution imaging while also achieving a large field of view (FOV), features which are both highly desirable in many practical applications such as nanoscale metrology[7–10] and bioimaging.[11,12] Although the ability to achieve high-resolution imaging over a large FOV can be accomplished on a conventional optical microscope by mechanically scanning the desired area through the focus of a high numerical aperture (NA) objective lens, this process requires complex mechanical manipulators and autofocusing features. Extensive work must be done to guarantee that the sample is always in focus as the stage moves, and a low speed is needed to maintain during the mechanical scan, adding to the complexity and cost of the technology and reducing the speed of analysis.

To address this critical issue, recent research into Fourier ptychography (FP) microscopes which utilize illumination control and computational-based postimaging processing has shown great potential in achieving both higher imaging resolution and a larger FOV while using a conventional optical microscope.[13–22] With this platform, arrays of LED light sources are used to replace the light illumination in a conventional optical microscope. LEDs are lit in sequence and a series of images are obtained at each LED illumination. The final, improved image is obtained from postimage processing by using an iterative phase retrieval algorithm.[23] As a comparison to traditional optical microscopy, a FP microscope with a 40×, 0.75 NA objective lens can generate an image with equivalent quality to that of an image from a 100×,1.45 NA oil-immersion objective lens.[24]

The FP is known as an indirect imaging method because the sample's spatial spectra are recorded on an imaging sensor, and a complex algorithm has to be applied to recover the true image. An alternative way to achieve direct imaging with both high resolution and a large FOV is to replace the high-NA objective with superior imaging items. Microsized dielectric particles have proven to be a promising candidate for replacing the high-NA objectives in modified microscopy systems. In fact, recent research has extensively explored the super-resolution capability of dielectric microparticles.[25–33] In these systems, dielectric microparticles are used as a "microlens", where the curvature of the bead serves to focus the light from the sample and amplify the image when used in combination with an objective lens. For example, a lateral resolution better than 50 nm has been achieved when using microparticles as an imaging lens in combination with an 80×, 0.9 NA objective.[34] Additionally, the imaging of plasmid DNA,[35,36] proteins,[37] and molecular beacons[38] with microparticles has been demonstrated. Moreover, single cells have been trapped and scanned with optical tweezers for creating optical nanoscopes.[39] A movable droplet as a microlens has also been demonstrated for subwavelength imaging.[40] However, most of these imaging examples are still limited to the small area around the focus of an individual microparticle, and a large FOV is hardly achievable when using a single microparticle.

To address these shortcomings, we introduce an acoustofluidic scanning nanoscope (AS-nanoscope), which can achieve subdiffraction-limit resolution and large FOV simultaneously. In the AS-nanoscope (Figure 1a), acoustofluidic technology is used to scan multiple microparticles on a sample surface.[41–64] Each microparticle serves as a high-NA

objective lens with a limited FOV (Figure 1b). The final large-FOV image of the sample is obtained by numerically combining the super-resolution images from each particle. The AS-nanoscope has the following exceptional features: (1) super resolution and large FOV (equivalent resolution to a 20×, 0.45 NA lens achieved with a 10×, 0.30 NA lens in combination with our acoustofluidic system); (2) autofocusing achieved by maintaining a constant working-distance from the surface topography of the sample (microparticles moving along the sample surface inherently maintain their position at the proper focal length); (3) direct imaging without complex phase retrieval algorithm (images are directly captured from each microparticle, and the assembled image is a numerical stitching of these photos, not an algorithmic generation).

RESULTS AND DISCUSSION

Characterization of Different Microparticles for the AS-Nanoscope.

Super resolution can be achieved by imaging with a microparticle because of the so-called "photonic jet" effect of the microparticle.[65–69] This effect can provide a focused beam waist which is smaller than the diffraction limit of light and can also enhance the backscattering of visible light. In order to develop our acoustofluidic scanning nanoscope, we first sought to determine the optical property of microparticles for leveraging the photonic jet effect to improve our resolution. To test the super-resolution imaging capability of different types of microparticles, we used a commercial Blu-ray disc with a 200 nm line width as the imaging target. Figure 2a shows the scanning electron microscopy (SEM) image of the structures on the Blu-ray disc. Figure S1 in the Supporting Information provides a relative size comparison of different imaging magnifications. The following microparticles were compared during testing: polystyrene (PS) microparticles with diameters of 10 μm (PS-10) and 20 μm (PS-20); barium titanate (BT) microparticles with diameters of 20 μm (BT-20) and 40 μm (BT-40). A mixture of all of these particles was diluted in deionized (DI) water (refractive index: 1.33), and a small drop of the solution was placed on the Blu-ray disc surface. A glass coverslip was then placed on top of the solution to form a flat surface and prevent solution evaporation. Figure 2b shows an optical image of the four types of particles, PS-10, PS-20, BT-20, and BT-40 marked as (d–g) in Figure 2b, respectively. The image of the particles was taken on a conventional microscope with an objective lens (20×, 0.45 NA) as schematically shown in Figure 2c. The parameter Z represents the focal height relative to the sample surface where the best image plane was achieved, as experimentally observed through the particle (Figure 2c). The Z-value changes with the image magnification of the microparticle, which is dependent on the size and refractive index of the microparticle.

The left panels in Figure 2d–g show the optical images of the structures on the Blu-ray disc that are captured using the four types of microparticles; the right panels show the simulated optical fields from the particles based on the finitedifference time-domain (FDTD) method (see Materials and Methods for more details).[70,71] The simulation clearly shows the photonic nanojet effect, wherein a plane wave is focused to subwavelength scales of nanojet waist (Figure S2 in the Supporting Information). Moreover, the resolution along a particular direction depends on the focal property of the microparticle in that particular direction. As an example, we have simulated the focus of a 2 μm PS bead along two orthogonal directions

with an FDTD method as shown in the Supporting Information Figure S3. These simulations indicated that the platform is capable of achieving super-resolution imaging of structures which are oriented in multiple directions. Figure 2h shows the line-profile of the four images as marked from the dashed lines in Figure 2d–g. Each line in Figure 2 from panel d to panel g provides the quantified visibility of the resolution of the nanostructures imaged through the particles. The resolution of a microsphere is governed by the waist width of the photonic nanojet, which is further determined by the size and refractive index of the microsphere.[26,33,34] Resolutions down to 50–100 nm have previously been achieved using microspheres.[26,33,34] In our experiments, Ge nanoparticles with a diameter of 100 nm were successfully imaged through a PS-20 microparticle, as shown in the Supporting Information Figure S4. The FOV of the AS-nanoscope is dependent on the objective lens used. The higher the NA of an objective lens used, the smaller the FOV. Visibility is used to quantitatively evaluate the quality of the images as calculated using the following equation

$$\text{Visibilty} = \frac{(I_{\max} - I_{\min})}{(I_{\max} + I_{\min})} \quad (1)$$

where $I_{\max}$ and $I_{\min}$ are the peak and trough intensity, respectively. A visibility of 0 and 1 correspond to the lowest and highest quality of imaging, respectively. The visibilities from the different images are 0.558, 0.589, 0.296, and 0.250 when using the PS-10, PS-20, BT-20, and BT-40 particles, respectively. The visibility depends on several parameters including the type of light illumination, type of microparticle, and type of target sample. The PS-20 particle shows the highest visibility among these four particles; based on these results, we chose the PS-20 particle to be used in future experiments.

The Effect of Different Objectives on Imaging Performance.

Having determined that the PS-20 particle provides the highest visibility, we explored the imaging capabilities when combining the particles with objective lenses of different magnification and NA. Figure 3a–d shows the images of the Blu-ray disc that have been imaged through a PS-20 particle under four different objectives, that is, (5×, NA = 0.15, FOV = 4.4 mm), (10×, NA = 0.30, FOV = 2.2 mm), (20×, NA = 0.45, FOV = 1.1 mm), and (50×, NA = 0.80, FOV = 0.44 mm), respectively. The PS-20 particle is placed on the boundary of the Blu-ray disc nanostructures, such that nanostructures are present under the right half of the spherical particle, and no nanostructures are present under the left half of the particle. Figure 3e–h shows the line-profiles of the optical images as marked with red and blue dashed lines. The red dashed lines pass through the images from the PS-20 particle (Z = 7.5 μm), while the blue dashed line passes through the images that are directly imaged with the objective lenses (Z = 0 μm). The fine nanostructures can be resolved by imaging through the PS-20 particle with a 10× or 20× objective lens (visibility of 0.600 and 0.649 for the 10× and 20× objective lenses, respectively). However, these features cannot be resolved when only using the objective lenses. The nanostructures can be resolved when solely using a 50× objective lens with a visibility of 0.159, but the presence of the PS-20 particle can further improve the visibility to 0.426. The fine nanostructures of the Blu-ray disk cannot be resolved with the 5× objective lens even with the presence of the PS-20 particle. Results for the visibility achieved using each imaging combination are provided in Table 1. From these

results, it is obvious that combining a PS-20 particle with either a 10× (FOV = 2.2 mm) or 20× (FOV = 1.1 mm) objective lens allows us to achieve both a large FOV as well as higher resolutions that cannot be realized with an objective lens in isolation. Moreover, the overall depth of field (DOF) of the AS-nanoscope is still limited to the DOF of the objective lens. A larger depth of field will guarantee all the images from the microparticles are still in focus. Because of the effects of gravity acting on the microsphere, the microsphere is expected to automatically follow the curvature of a sample surface as it is moved. A rough sample surface consisting of 100 nm Ge nanoparticles was successfully imaged from two separate PS-20 at two different positions, as shown in the Supporting Information Figure S4.

The Effect of Illumination on the Imaging Quality.

Illumination can play an important role in determining the overall imaging quality when using an optical microscope. Thus, we experimented with two different types of illumination (transmission mode and reflection mode) to determine the optimal method for improving imaging performance. In the transmission mode, the illuminating light is first transmitted through the nanostructures and then passes through the PS-20 particle and exits through the 10× objective lens. In the reflection mode, the illuminating light first passes through the 10× objective lens and then through the PS-20 particle. The light is then reflected off of the sample and collected by the same PS-20 particle before returning to the 10× objective lens. Figure 4a,b shows optical images of the same nanostructures that have been imaged through a PS-20 particle with a 10× objective lens in the transmission and reflection illumination modes, respectively. Because the Blu-ray disk does not transmit green light, a grating pattern consisting of 800 nm wide chrome lines on a glass substrate (Micro Lithography Services Ltd., U.K.) was used for the experiments in this section. Under the same experimental condition, improved imaging quality is obtained when using the transmission mode, as seen by comparing panels a and b in Figure 4, and as shown in the line-profile in Figure 4c. The red and blue dotted lines show the line-profiles from the images shown in Figure 4a,b, as marked by the red and blue dashed lines, respectively. The same result is observed in the use of a 20× objective lens as shown in Figure 4d,e; these images show the corresponding images generated when using the transmission and reflection modes to analyze the same nanostructure with a 20× objective lens. Figure 4f shows the line-profile from the images shown in Figure 4d,e as marked by the red and blue dashed lines, respectively. In both cases, the images in transmission modes have a higher visibility (0.684, 10× and 0.664, 20×) than that of the reflection mode (0.182, 10× and 0.356, 20×). This phenomenon is likely caused by the fact that the double-light passing through the PS-20 particle in the reflection mode produces larger aberrations than that of a single-light passing through the particle in the transmission mode (Supporting Information Figure S5).

Acoustofluidic Scanning System.

Even though a static PS-20 particle can be used to significantly improve the resolution of a conventional microscope, its maximum FOV is limited to the physical diameter of the microparticle. To overcome this limitation, we designed an acoustofluidic scanning system that allows us to simultaneously scan multiple PS-20 particles across a 2.2 mm FOV size with a 10× objective lens; the combination of the microparticles with the 10× objective achieves the same FOV as the standard 10× objective but offers the same resolution as a 20×

objective. We use the acoustofluidic device to translate the particles and capture high-resolution images of the entire FOV without moving the objective, as opposed to requiring manual FOV manipulation or integrating a costly automated mechanical scanning device. It should be noted that other methods, such as hydrodynamic forces, could also be used to move the microparticles for scanning. Acoustic waves were chosen in this work because it is convenient to load the microparticles onto the sample and integrate the acoustic transducer for programmable and real-time particle manipulation. The acoustofluidic scanning device (Figure 5b, top) utilizes a low-cost (~$1) piezoelectric transducer that is bonded on the top surface of a glass coverslip to generate flexural mode acoustic waves in the coverslip. The target sample to be imaged is placed under the bottom surface of the coverslip with a thin fluid layer with microparticles being contained between them, as shown in Figure 1. The excitation voltage signal for the piezoelectric transducer, which is generated by a function generator (AFG 3011, Tektronix), contains sine waves in a burst mode with a duty cycle of 50% and a burst rate of 0.5 Hz, as shown in Figure 5a. Upon excitation, the acoustofluidic scanning device can generate flexural mode acoustic waves in the glass coverslip; the wave energy further transmits into the fluid layer under the bottom surface of the coverslip to push the microparticles forward along the wave propagation direction. The three optical images from (i) to (iii) in Figure 5a show that a PS-20 particle (marked in a white circle) is pushed away by the acoustic wave every two seconds.

To visualize the acoustic waves generated by the acoustofluidic device, simulations are performed using the finite element software COMSOL Multiphysics (see Materials and Methods). The finite element model is built using the piezoelectric multiphysics, solid mechanics, and electrostatics modules. Using a time-domain study, we are able to visualize the acoustic waves that are generated by the piezoelectric transducer which are transmitted into the fluid layer between the glass coverslip and the target sample to be imaged. Figure 5b (bottom) shows the simulated wavefield on the glass coverslip layer; it can be seen that the generated waves propagate away from the transducer where they cause streaming in the fluid beneath the coverslip, which moves the PS-20 particles for the scanning process.

To investigate the scanning efficiency, we experimentally characterized the particle-moving ratio, which is defined as the number of moving particles divided by the total number of particles per activation period (period of the burst) of the transducer. In this experiment, PS-20 particles in DI water are added between the glass coverslip and the target sample to be imaged. The excitation voltage for the piezoelectric transducer is kept at 3 V_{pp}, while the frequency of the excitation sine signal is swept from 100 Hz to 4 kHz with an increment of 100 Hz. The number of particles that move under influence from the acoustic wave is imaged and counted with a 10× objective lens. The experiment is repeated three times in the same experimental condition. Recorded image frames were processed by using the ImageJ software. Figure 5c plots the particle ratio with respect to the excitation frequency, showing that the highest particle-moving ratio of 93% can be achieved at 2.1 kHz. Figure 5d shows a stacked image acquired during the moving of the PS-20 particles. The stacked image shows that most of the particles move in the same direction as the propagation direction of the acoustic wave (Supporting Information, Video 1). Although a higher flow speed and a denser particle loading can lead to increased imaging speed, these factors may also lead to

image blurring and particle overlapping. Therefore, a trade-off has to be made between the imaging speed and the flow speed and particle density.

Image Processing When Using the AS-Nanoscope.

Using moving microparticles, a series of nanoscale-resolution images corresponding to different positions of particles can be acquired; moving the microparticles ensures that a high-resolution image of each area within the FOV can be obtained. Stitching all of the acquired images together generates a high-resolution image over a large FOV. To experimentally demonstrate the capability of the AS-nanoscope, a target sample with the word “DUKE” was fabricated on a glass mask with 800 nm wide chrome grating lines and 800 nm spaces between adjacent features. A video was captured on a normal color CCD camera as the letter “DUKE” is imaged with the moving PS-20 particles and a 10× objective. A MATLAB image-processing tool was developed to process the images in the video and to form the final image with a high resolution and large FOV. The image-processing tool includes two parts: (1) particle recognition and position identification; and (2) recursive image merging. First, we developed a particle recognition algorithm which includes particle locating, cropping, and pasting, as demonstrated in the left panel of Figure 6a. At the same time, the central positions of each particle (x, y) relative to the imaging sample are automatically retrieved, which will be used during the image merging process. Microparticle images are pasted into the final image by specific αx and αy coordination. $\alpha = \gamma/\beta = 1.52$ is the magnification factor that is obtained from the pitch ratio between the real image and virtual image as shown in the right panel of Figure 6a. Second, we designed a recursive image merging algorithm that can merge the scanned images captured through the microparticles. In the left panel of Figure 6b, red arrows show trajectories of six PS-20 particles. The final merged image from the six moving PS-20 particles are formed by applying the recursive image merging algorithm as shown in the right panel of Figure 6b (Supporting Information, Video 2). For this merged image, 100 image frames were processed. Figure 6c represents the image construction process of the letter “D” as the number of frames increases from 5 to 1,000; as more frames are used to form the merged image, a successively more complete letter is formed. The top and bottom rows of Figure 6d show the scanned images of the word “DUKE” based on our acoustofluidic method, and using a 10× objective in isolation, respectfully. Each image generated with the acoustofluidic method consists of 3500 image frames, which covers 99% of the imaged area (Table S1 in the Supporting Information). The image in the red boxes (i) and (ii) of Figure 6d provide close-ups of parts of the letter “K”. The fine detail of the letter is well resolved when using the acoustofluidic method, as opposed to boxes (iii) and (iv) which provide images from the 10× objective lens. In this experiment, the PS-20 particles in combination with the 10× objective lens (NA = 0.3, visibility of 0.682) have a resolving power similar to a 20× objective lens (NA = 0.45, visibility of 0.664) but has much larger FOV than that of a 20× objective lens. The FOV of the AS-nanoscope is only limited by the field view of the 10× objective lens, which is 2 times larger than the 20× objective lens (Figure S6 in the Supporting Information).

CONCLUSION

In this work we have documented the development of an AS-nanoscope that can achieve both high resolution and large FOV at the same time, which alleviates a long-existing shortcoming of conventional microscopes. The AS-nanoscope developed here can serve as either an add-on component to expand the capability of a conventional microscope, or could be paired with low-cost imaging platforms to develop a stand-alone microscope for portable imaging. The AS-nanoscope achieves high-resolution imaging without the need for conventional high-cost and bulky objectives with high NAs. The FOV of the AS-nanoscope is much larger than that from a conventional high-NA objective lens, and it is able to achieve the same resolving power. The AS-nanoscope automatically focuses and maintains a constant working distance during the scanning process thanks to the interaction of the microparticles with the liquid domain. The resolving power of the AS-nanoscope can easily be adjusted by using microparticles of different sizes and refractive indices. Additionally, it may be possible to further improve the performance of this platform by exploring additional microparticle sizes and materials, in combination with various objectives. Altogether, we believe this AS-nanoscope has the potential to be integrated into a wide range of applications from portable nanodetection to biomedicine and microfluidics.

MATERIALS AND METHODS

Simulation for Photonic Nanojets.

Propagation of near-field electromagnetic wave was simulated by using finite-difference time-domain method. Monochromatic incident light with 532 nm was propagated along the positive *x*-axis. Cylindrical model for microparticle with refractive index (PS, 1.6; BT, 2.2) in different radius and surrounding medium with refractive index (water, 1.33) were applied.

Device Fabrication and Experimental Setup.

An acoustic transducer (AB2720B-LW100-R, PUI Audio, Inc., U.S.A.) is bonded by epoxy (PermaPoxyTM 5 min General Purpose, Permatex, U.S.A.) onto a cover glass slide (24 × 60 mm No.0–3223, Erie Scientific LLC., U.S.A.). Microparticles are mixed with deionized water and drop cast to the sample surface. During the experiment, the volume of the microparticle solution was fixed to 20 μL to keep the consistency of the height of the water channel between the sample and cover glass. The sample is placed on an upright microscope (Eclipse LV100, Nikon, Japan). To minimize chromatic aberration, colored glass bandpass filter (FGV9 - Ø25 mm VG9, Thorlabs, U.S.A.) was used for the light illumination.

Microparticle Preparation.

To verify the super-resolution performance by the microparticle in different refractive indices, we choose polystyrene (PS, refractive index, 1.6, Sigma-Aldrich, U.S.A.) and barium titanate (BT, refractive index, 2.2, Cospheric, U.S.A.) microparticles in different sizes: 10 μm PS, 20 μm PS, 20 μm BT, and 40 μm BT, respectively. The microparticles are diluted before drop cast on the sample.

Simulation of Acoustic Streaming.

In order to better understand the acoustic streaming occurring beneath the glass slide, a detailed model of the acoustofluidic device was created in Comsol Multiphysics (version 5.3). The model incorporated the glass coverslip, epoxy bonding layer, and dual layer transducer (brass base and piezoelectric disc) to increase the similarity between experimental and numerical setups. Material properties were applied to different components using the materials library in Comsol. A time domain study was used to visualize the transducer excitation and subsequent waves generated in the glass coverslip. Utilizing the electrostatics module, a 2 kHz, 1 V oscillatory signal was applied to the transducer. The piezoelectric multiphysics module coupled the electrostatic solution with the solid mechanics module. A low reflection boundary layer condition was applied to either end of the glass slide, which we found to produce a vibration profile that was qualitatively consistent with previous experimental findings and sufficient for understanding the acoustic streaming within the device.

SEM Imaging of Nanopattern.

To verify the nanopattern on the Blu-ray disc, we used a scanning electron microscope (Hitachi TM3030 Plus Tabletop, Japan). Before the experiment, we uncovered the protection film from the Blu-ray disc and took an SEM image with 6000× magnification.

Supplementary Material

Refer to Web version on PubMed Central for supplementary material.

ACKNOWLEDGMENTS

We acknowledge support from the National Institutes of Health (UG3TR002978, R01GM132603, R33CA223908, R01GM127714, R01GM135486, and R43AG063643), United States Army Medical Research Acquisition Activity (W81XWH-18-1-0242), and National Science Foundation (CMMI-1761132; ECCS-1807601).

REFERENCES

(1). Dixon A; Damaskinos S; Atkinson M A Scanning Confocal Microscope for Transmission and Reflection Imaging. Nature 1991, 351, 551.

(2). Betzig E; Trautman JK Near-Field Optics: Microscopy, Spectroscopy, and Surface Modification beyond the Diffraction Limit. Science 1992, 257, 189–195. [PubMed: 17794749]

(3). McMullan D An Improved Scanning Electron Microscope for Opaque Specimens. Proc. Inst. Electr. Eng., Part 2 1953, 100, 245–256.

(4). Seiler H Secondary Electron Emission in the Scanning Electron Microscope. J. Appl. Phys 1983, 54, R1–R18.

(5). Meyer G; Amer NM Novel Optical Approach to Atomic Force Microscopy. Appl. Phys. Lett 1988, 53, 1045–1047.

(6). Reimer L Elements of a Transmission Electron Microscope In Transmission Electron Microscopy: Physics of Image Formation and Microanalysis; Arthur LS, Jay ME, Koichi S, David LM, Theodor T, Eds.; Springer: New York, 2013; Vol. 36, pp 86–133.

(7). Imtiaz A; Wallis TM; Kabos P Near-Field Scanning Microwave Microscopy: An Emerging Research Tool for Nanoscale Metrology. IEEE Microwave Mag 2014, 15, 52–64.

(8). Gruhlke M; Rothe H Combining Coordinate Measurement and Nanometrology for Large-Range Nanoscale Metrology, Instrumentation, Metrology, and Standards for Nanomanufacturing; 9 10, 2007; International Society for Optics and Photonics: San Diego, 2007; p 66480I.

(9). Ray A; Khalid MA; Demčenko A; Daloglu M; Tseng D; Reboud J; Cooper JM; Ozcan A Holographic Detection of Nanoparticles Using Acoustically Actuated Nanolenses. Nat. Commun 2020, 11, 1–10.

(10). Canady TD; Li N; Smith LD; Lu Y; Kohli M; Smith AM; Cunningham BT Digital-Resolution Detection of Microrna with Single-Base Selectivity by Photonic Resonator Absorption Microscopy. Proc. Natl. Acad. Sci. U. S. A 2019, 116, 19362–19367. [PubMed: 31501320]

(11). Abdelhady HG; Allen S; Ebbens SJ; Madden C; Patel N; Roberts CJ; Zhang J Towards Nanoscale Metrology for Biomolecular Imaging by Atomic Force Microscopy. Nanotechnology 2005, 16, 966.

(12). Farkas DL Invention and Commercialization in Optical Bioimaging. Nat. Biotechnol 2003, 21, 1269–1271. [PubMed: 14595349]

(13). Zheng G; Horstmeyer R; Yang C Wide-Field, High-Resolution Fourier Ptychographic Microscopy. Nat. Photonics 2013, 7, 739. [PubMed: 25243016]

(14). Tian L; Li X; Ramchandran K; Waller L Multiplexed Coded Illumination for Fourier Ptychography with an Led Array Microscope. Biomed. Opt. Express 2014, 5, 2376–2389. [PubMed: 25071971]

(15). Horstmeyer R; Chen RY; Ou X; Ames B; Tropp JA; Yang C Solving Ptychography with a Convex Relaxation. New J. Phys 2015, 17, 053044.

(16). Faulkner HML; Rodenburg J Movable Aperture Lensless Transmission Microscopy: A Novel Phase Retrieval Algorithm. Phys. Rev. Lett 2004, 93, 023903. [PubMed: 15323918]

(17). Rodenburg JM; Faulkner HM A Phase Retrieval Algorithm for Shifting Illumination. Appl. Phys. Lett 2004, 85, 4795–4797.

(18). Maiden AM; Rodenburg JM An Improved Ptychographical Phase Retrieval Algorithm for Diffractive Imaging. Ultramicroscopy 2009, 109, 1256–1262. [PubMed: 19541420]

(19). Maiden AM; Humphry MJ; Rodenburg J Ptychographic Transmission Microscopy in Three Dimensions Using a Multi-Slice Approach. J. Opt. Soc. Am. A 2012, 29, 1606–1614.

(20). Ou X; Zheng G; Yang C Embedded Pupil Function Recovery for Fourier Ptychographic Microscopy. Opt. Express 2014, 22, 4960–4972. [PubMed: 24663835]

(21). Horstmeyer R; Chung J; Ou X; Zheng G; Yang C Diffraction Tomography with Fourier Ptychography. Optica 2016, 3, 827–835. [PubMed: 28736737]

(22). Horstmeyer R; Yang C A Phase Space Model of Fourier Ptychographic Microscopy. Opt. Express 2014, 22, 338–358. [PubMed: 24514995]

(23). Yeh L-H; Dong J; Zhong J; Tian L; Chen M; Tang G; Soltanolkotabi M; Waller L Experimental Robustness of Fourier Ptychography Phase Retrieval Algorithms. Opt. Express 2015, 23, 33214–33240. [PubMed: 26831989]

(24). Ou X; Horstmeyer R; Zheng G; Yang C High Numerical Aperture Fourier Ptychography: Principle, Implementation and Characterization. Opt. Express 2015, 23, 3472–3491. [PubMed: 25836203]

(25). Yang H; Moullan N; Auwerx J; Gijs MA Super-Resolution Biological Microscopy Using Virtual Imaging by a Microsphere Nanoscope. Small 2014, 10, 1712–1718. [PubMed: 24914446]

(26). Yang H; Trouillon R; Huszka G; Gijs MA Super-Resolution Imaging of a Dielectric Microsphere Is Governed by the Waist of Its Photonic Nanojet. Nano Lett. 2016, 16, 4862–4870. [PubMed: 27398718]

(27). Darafsheh A Influence of the Background Medium on Imaging Performance of Microsphere-Assisted Super-Resolution Microscopy. Opt. Lett 2017, 42, 735–738. [PubMed: 28198852]

(28). Zhang T; Li P; Yu H; Wang F; Wang X; Yang T; Yang W; Li WJ; Wang Y; Liu L Fabrication of Flexible Microlens Arrays for Parallel Super-Resolution Imaging. Appl. Surf. Sci 2020, 504, 144375.

(29). Bezryadina A; Li J; Zhao J; Kothambawala A; Ponsetto J; Huang E; Wang J; Liu Z Localized Plasmonic Structured Illumination Microscopy with an Optically Trapped Microlens. Nanoscale 2017, 9, 14907–14912. [PubMed: 28949360]

(30). Chang C-W; Li P-Y; Tsao Y; Chu S-W Coherent Superresolution Assisted by Surface Plasmons and the Role of Dielelctric Microlenses, Plasmonics: Design, Materials, Fabrication, Characterization, and Applications XVI; International Society for Optics and Photonics, 9 19, 2018, San Diego, 2018; p 107220E.

(31). Brettin A; McGinnis CL; Abolmaali F; Limberopoulos NI; Walker D; Urbas AM; Poffo L; Maslov AV; Astratov VN Superresolution Imaging of Fluorescent Nanospheres by Using High-Index Microspheres Embedded in Slabs with Illumination Provided by Plasmonic Array NAECON 2018-IEEE National Aerospace and Electronics Conference; 7 23, 2018; IEEE: Dayton, 2018; pp 536–539.

(32). Yang S; Cao Y; Shi Q; Wang X; Chen T; Wang J; Ye Y-H Label-Free Super-Resolution Imaging of Transparent Dielectric Objects Assembled on a Silver Film by a Microsphere-Assisted Microscope. J. Phys. Chem. C 2019, 123, 28353–28358.

(33). Wang Z; Joseph N; Li L; Luk'Yanchuk B A Review of Optical Near-Fields in Particle/Tip-Assisted Laser Nanofabrication. Proc. Inst. Mech. Eng., Part C 2010, 224, 1113–1127.

(34). Wang Z; Guo W; Li L; Luk'yanchuk B; Khan A; Liu Z; Chen Z; Hong M Optical Virtual Imaging at 50 Nm Lateral Resolution with a White-Light Nanoscope. Nat. Commun 2011, 2, 218. [PubMed: 21364557]

(35). Li Y; Xin H; Liu X; Zhang Y; Lei H; Li B Trapping and Detection of Nanoparticles and Cells Using a Parallel Photonic Nanojet Array. ACS Nano 2016, 10, 5800–5808. [PubMed: 27163754]

(36). Li Y-C; Xin H-B; Lei H-X; Liu L-L; Li Y-Z; Zhang Y; Li B-J Manipulation and Detection of Single Nanoparticles and Biomolecules by a Photonic Nanojet. Light: Sci. Appl 2016, 5, No. e16176. [PubMed: 30167133]

(37). Brettin A; Blanchette KF; Nesmelov Y; Limberopoulos NI; Urbas AM; Astratov VN Microsphere Nanoscopy for Imaging of Actin Proteins, 2016 IEEE National Aerospace and Electronics Conference (NAECON) and Ohio Innovation Summit (OIS); 7 25, 2016; IEEE: Dayton, 2016; pp 269–271.

(38). Teng F; Libera M Microlens Enhancement of Surface-Tethered Molecular Beacons. Langmuir 2018, 34, 14969–14974. [PubMed: 30277788]

(39). Li Y; Liu X; Li B Single-Cell Biomagnifier for Optical Nanoscopes and Nanotweezers. Light: Sci. Appl 2019, 8, 1–12. [PubMed: 30622704]

(40). Chen X; Wu T; Gong Z; Li Y; Zhang Y; Li B Subwavelength Imaging and Detection Using Adjustable and Movable Droplet Microlenses. Photonics Res. 2020, 8, 225–234.

(41). Ozcelik A; Rufo J; Guo F; Gu Y; Li P; Lata J; Huang TJ Acoustic Tweezers for the Life Sciences. Nat. Methods 2018, 15, 1021. [PubMed: 30478321]

(42). Ahmed H; Park J; Destgeer G; Afzal M; Sung HJ Surface Acoustic Wave-Based Micromixing Enhancement Using a Single Interdigital Transducer. Appl. Phys. Lett 2019, 114, 043702.

(43). Bruus H Acoustofluidics 7: The Acoustic Radiation Force on Small Particles. Lab Chip 2012, 12, 1014–1021. [PubMed: 22349937]

(44). Collins DJ; Alan T; Helmerson K; Neild A Surface Acoustic Waves for On-Demand Production of Picoliter Droplets and Particle Encapsulation. Lab Chip 2013, 13, 3225–3231. [PubMed: 23784263]

(45). Collins DJ; O'Rorke R; Neild A; Han J; Ai Y Acoustic Fields and Microfluidic Patterning around Embedded Micro-Structures Subject to Surface Acoustic Waves. Soft Matter 2019, 15, 8691–8705. [PubMed: 31657435]

(46). Cox L; Melde K; Croxford A; Fischer P; Drinkwater BW Acoustic Hologram Enhanced Phased Arrays for Ultrasonic Particle Manipulation. Phys. Rev. Appl 2019, 12, 064055.

(47). Delsing P; Cleland AN; Schuetz MJ; Knörzer J; Giedke G; Cirac JI; Srinivasan K; Wu M; Balram KC; Bäuerle C; et al. The 2019 Surface Acoustic Waves Roadmap. J. Phys. D: Appl. Phys 2019, 52, 353001.

(48). Friend J; Yeo LY Microscale Acoustofluidics: Microfluidics Driven via Acoustics and Ultrasonics. Rev. Mod. Phys 2011, 83, 647.

(49). Gautam GP; Burger T; Wilcox A; Cumbo MJ; Graves SW; Piyasena ME Simple and Inexpensive Micromachined Aluminum Microfluidic Devices for Acoustic Focusing of Particles and Cells. Anal. Bioanal. Chem 2018, 410, 3385–3394. [PubMed: 29651523]

(50). Kadimisetty K; Song J; Doto AM; Hwang Y; Peng J; Mauk MG; Bushman FD; Gross R; Jarvis JN; Liu C Fully 3d Printed Integrated Reactor Array for Point-of-Care Molecular Diagnostics. Biosens. Bioelectron 2018, 109, 156–163. [PubMed: 29550739]

(51). Lin T-Y; Do T; Kwon P; Lillehoj PB 3D Printed Metal Molds for Hot Embossing Plastic Microfluidic Devices. Lab Chip 2017, 17, 241–247. [PubMed: 27934978]

(52). O'Rorke R; Winkler A; Collins D; Ai Y Slowness Curve Surface Acoustic Wave Transducers for Optimized Acoustic Streaming. RSC Adv. 2020, 10, 11582–11589.

(53). Reboud J; Bourquin Y; Wilson R; Pall GS; Jiwaji M; Pitt AR; Graham A; Waters AP; Cooper JM Shaping Acoustic Fields as a Toolset for Microfluidic Manipulations in Diagnostic Technologies. Proc. Natl. Acad. Sci. U. S. A 2012, 109, 15162–15167. [PubMed: 22949692]

(54). Shaglwf Z; Hammarström B; Shona Laila D; Hill M; Glynne-Jones P Acoustofluidic Particle Steering. J. Acoust. Soc. Am 2019, 145, 945–955. [PubMed: 30823821]

(55). Tao R; Hasan S; Wang HZ; Zhou J; Luo JT; McHale G; Gibson D; Canyelles-Pericas P; Cooke MD; Wood D; et al. Bimorph Material/Structure Designs for High Sensitivity Flexible Surface Acoustic Wave Temperature Sensors. Sci. Rep 2018, 8, 1–9. [PubMed: 29311619]

(56). Tung K-W; Chung P-S; Wu C; Man T; Tiwari S; Wu B; Chou Y-F; Yang F.-l.; Chiou P-Y Deep, Sub-Wavelength Acoustic Patterning of Complex and Non-Periodic Shapes on Soft Membranes Supported by Air Cavities. Lab Chip 2019, 19, 3714–3725. [PubMed: 31584051]

(57). Van Assche D; Reithuber E; Qiu W; Laurell T; Henriques-Normark B; Mellroth P; Ohlsson P; Augustsson P Gradient Acoustic Focusing of Sub-Micron Particles for Separation of Bacteria from Blood Lysate. Sci. Rep 2020, 10, 1–13.

(58). Li P; Huang TJ Applications of Acoustofluidics in Bioanalytical Chemistry. Anal. Chem 2019, 91, 757–767. [PubMed: 30561981]

(59). Wu M; Ozcelik A; Rufo J; Wang Z; Fang R; Huang TJ Acoustofluidic Separation of Cells and Particles. Microsyst. Nanoeng 2019, 5, 32. [PubMed: 31231539]

(60). Zhang SP; Lata J; Chen C; Mai J; Guo F; Tian Z; Ren L; Mao Z; Huang P-H; Li P; Yang S; Huang TJ Digital Acoustofluidics Enables Contactless and Programmable Liquid Handling. Nat. Commun 2018, 9, 2928. [PubMed: 30050088]

(61). Tian Z; Yang S; Huang P-H; Wang Z; Zhang P; Gu Y; Bachman H; Chen C; Wu M; Xie Y; Huang TJ Wave Number–Spiral Acoustic Tweezers for Dynamic and Reconfigurable Manipulation of Particles and Cells. Sci. Adv 2019, 5, No. eaau6062. [PubMed: 31172021]

(62). Tian Z; Shen C; Li J; Reit E; Bachman H; Socolar JE; Cummer SA; Huang TJ Dispersion Tuning and Route Reconfiguration of Acoustic Waves in Valley Topological Phononic Crystals. Nat. Commun 2020, 11, 1–10.

(63). Nama N; Huang P-H; Huang TJ; Costanzo F Investigation of Acoustic Streaming Patterns around Oscillating Sharp Edges. Lab Chip 2014, 14, 2824–2836. [PubMed: 24903475]

(64). Ahmed D; Chan CY; Lin S-CS; Muddana HS; Nama N; Benkovic SJ; Huang TJ Tunable, Pulsatile Chemical Gradient Generation *via* Acoustically Driven Oscillating Bubbles. Lab Chip 2013, 13, 328–331. [PubMed: 23254861]

(65). Chen Z; Taflove A; Backman V Photonic Nanojet Enhancement of Backscattering of Light by Nanoparticles: A Potential Novel Visible-Light Ultramicroscopy Technique. Opt. Express 2004, 12, 1214–1220. [PubMed: 19474940]

(66). Ferrand P; Wenger J; Devilez A; Pianta M; Stout B; Bonod N; Popov E; Rigneault H Direct Imaging of Photonic Nanojets. Opt. Express 2008, 16, 6930–6940. [PubMed: 18545397]

(67). Li X; Chen Z; Taflove A; Backman V Optical Analysis of Nanoparticles via Enhanced Backscattering Facilitated by 3-D Photonic Nanojets. Opt. Express 2005, 13, 526–533. [PubMed: 19488381]

(68). Itagi A; Challener W Optics of Photonic Nanojets. J. Opt. Soc. Am. A 2005, 22, 2847–2858.

(69). Duan Y; Barbastathis G; Zhang B Classical Imaging Theory of a Microlens with Super-Resolution. Opt. Lett 2013, 38, 2988–2990. [PubMed: 24104628]

(70). Bohren CF; Huffman DR Absorption and Scattering by a Sphere In Absorption and Scattering of Light by Small Particles; John Wiley & Sons: Weinheim, 2008; pp 83–129.

(71). Schäfer J-P Implementierung Und Anwendung Analytischer Und Numerischer Verfahren Zur Lösung Der Maxwellgleichungen Für Die Untersuchung Der Lichtausbreitung in Biologischem Gewebe. Doctorate Dissertation, University of Ulm, Ulm Germany, 6 30, 2011.

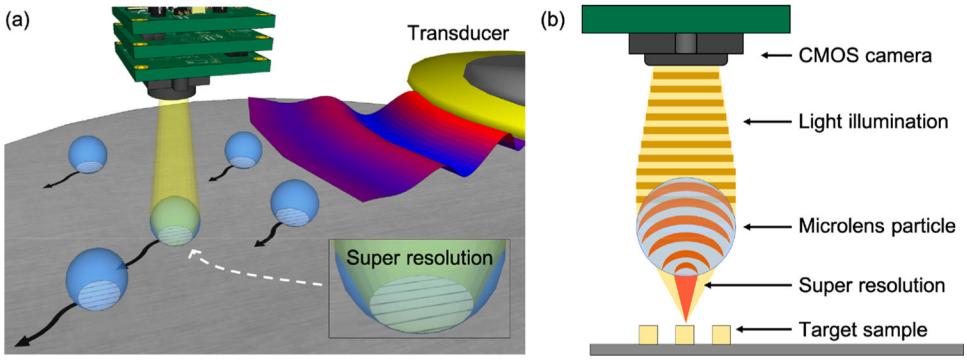

Figure 1.

Schematic of the AS-nanoscope. (a) Flexural acoustic waves are transmitted by the piezoelectric transducer for microparticle manipulation during the scanning process. Microparticles can achieve super-resolution effects to resolve nanometer-sized features. (b) The 2D schematic of the super-resolution effect utilized in the acoustofluidic scanning nanoscope.

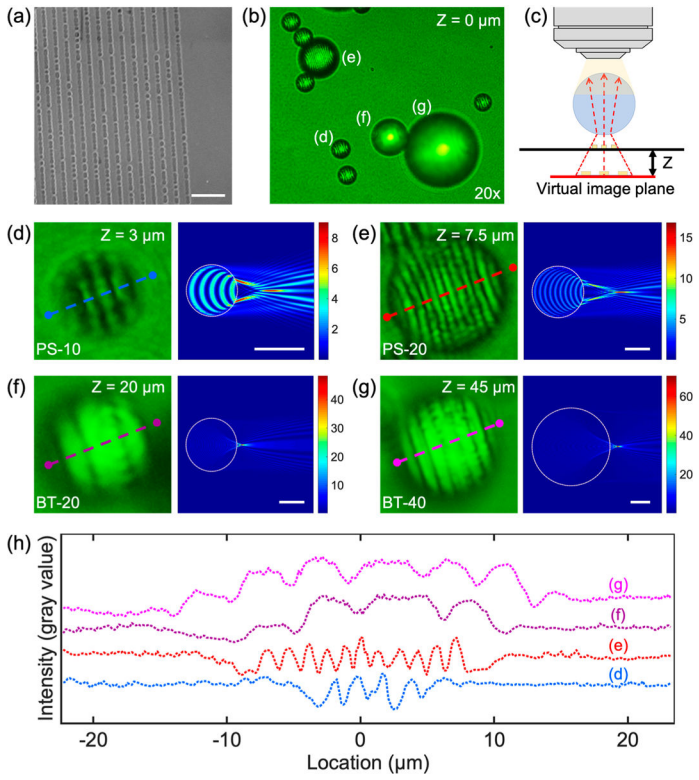

Figure 2.

Optical analysis of different materials and sizes of microparticles used in the AS-nanoscope. (a) SEM image of the surface of a Bluray disc which has sub-500 nm nanostructures. The scale bar is 1 μm. (b) Cropped photo of the particles of different size and material investigated for their photonic jet effect, as captured by a 20× microscope objective. (c) A visual explanation of Z-parameter, which describes the focal distance between the substrate surface and virtual image plane. (d) Magnified nanostructure shape as captured through different microparticles at their optimal Z-values (left). Simulation results of the electromagnetic radiation of an infinite circular cylinder based on a finite-difference time-domain method (right) for a (d) 10 μm PS (PS-10) particle, (e) 20 μm PS (PS-20) particle, (f) 20 μm barium titanate (BT-20) solid glass particle, and (g) 40 μm BT (BT-40) particle. The scale bars are 10 μm. (h) Pixel line intensity profile comparing the particles from (d–g). In the graph, the center of each particle is represented by 0 μm.

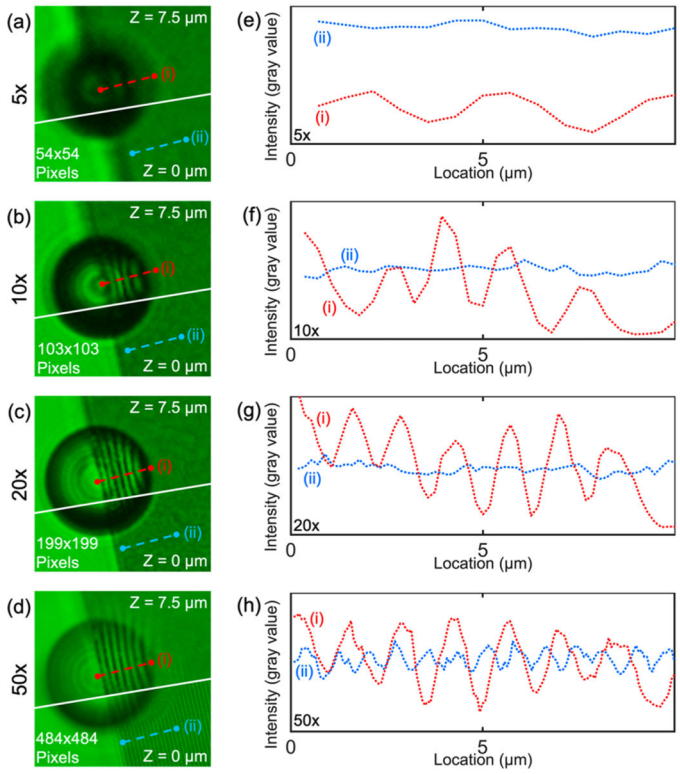

Figure 3.

Comparison of optical resolutions of nanostructures on a Blu-ray disc when using a PS-20 microparticle with different magnifications of the microscope objective. (a) PS-20 microparticle (top) on a Blu-ray disc in the same region of interest but at a different Z value as the image taken with just the objective lens (bottom). The nanostructure is best focused through the microparticle when Z is 7.5 μm (top) and focused without the microparticle when Z is 0 μm (bottom) for the 5× microscope objective. (b) 10×, (c) 20×, (d) 50× objective imaging results respectively. (e) Line plot profile of the nanostructures captured at different focal distances (i) through the microparticle and (ii) without the microparticle using a 5× objective. (f) 10×, (g) 20×, (h) 50× objective imaging results, respectively.

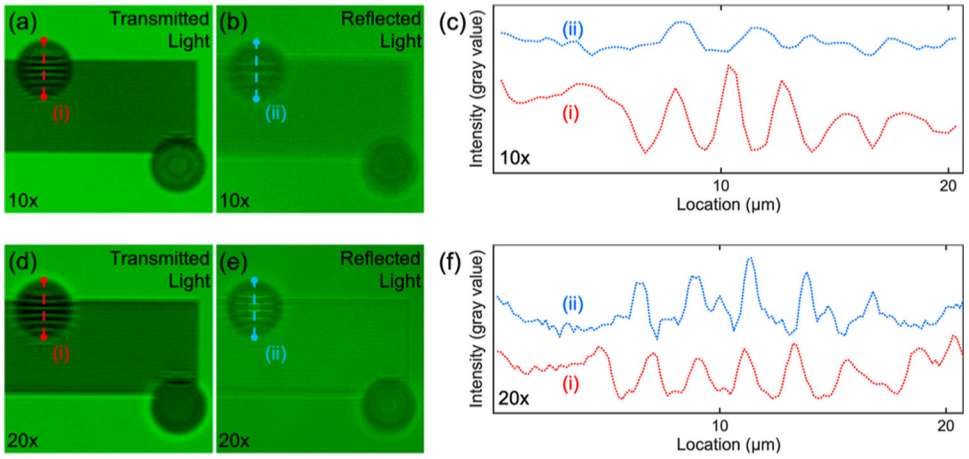

Figure 4.

Resolution comparison between transmitted light and reflected light passing through the microparticles using 10× and 20× microscope objectives. 800 nm chrome grating patterns are resolved using PS-20 microparticles and (a) transmitted light or (b) reflected light with a 10× microscope objective. (c) Line plot profiles of the 800 nm chrome grating patterns extracted when using transmitted light (i) or reflected light (ii). (d–f) Same comparison using a 20× microscope objective.

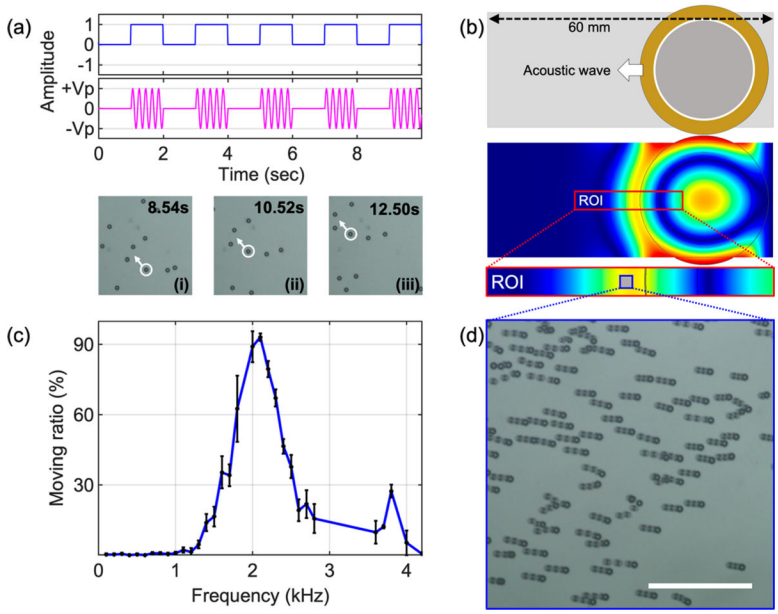

Figure 5.

Acoustofluidic particle manipulation. (a, top) Illustration of the burst mode excitation with a duty cycle of 50% and a burst period of 2 s. (a, bottom) Time-lapse images acquired every 2 s after the completion of each burst. (b, top) Schematic figure of the acoustofluidic device composed of a circular piezoelectric transducer bonded onto a glass coverslip. (b, bottom) COMSOL simulation result of the acoustic field in the coverslip. Waves propagate out from the transducer, pushing particles in the fluid domain. (c) Relationship between moving particle ratio and excitation frequency under a 3 V_{pp} amplitude excitation. (d) Stacked image of PS-20 particle movement. The imaging area corresponds to the blue box area in (b). The scale bar is 300 μm.

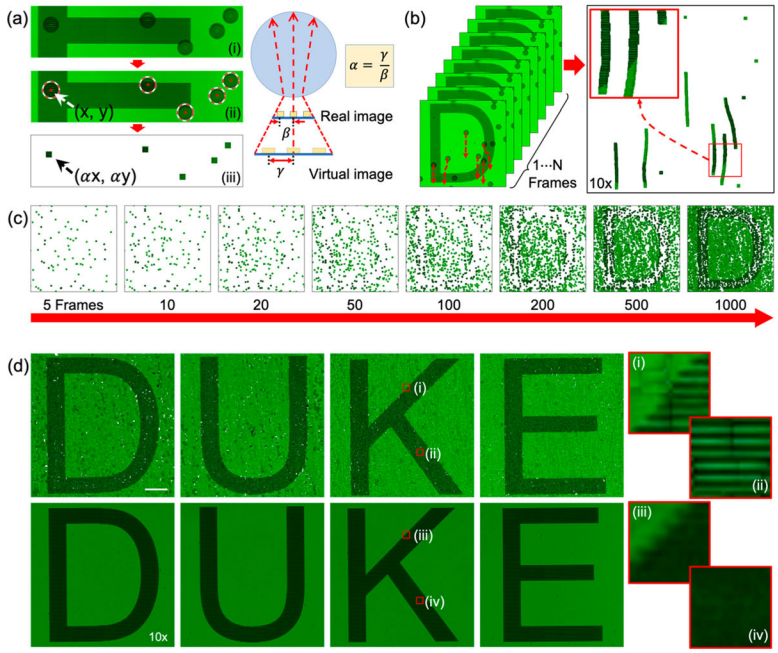

Figure 6.

Image processing procedure for automatic 2D scanning through acoustofluidic microparticle manipulation. (a-ii) Selective microparticle image cropping and pasting by using a circle finding procedure in MATLAB. Microparticles are searched by (ii) an automated circle finding algorithm and pasted into (iii) a final result image based on their α-value. The α-value is determined by a ratio between real image intensity and virtual image intensity as shown in the right side of the figure. (b) By using a circle finding function, a 2D line grating image is generated by following a microparticle's movement. (c) Scanned letter "D" images generated with different numbers of image frames from 5 to 1000. (d) (top) Scanned 2D images of the word "DUKE" using PS-20 microparticles and a 10× microscope objective; (bottom) 10× microscope objective photo of the same word. Red boxes (i) and (ii) show magnified images in scanned letter "K", and red boxes (iii) and (iv) show the same region of interest captured with a 10× microscopic objective. The scale bar is 50 μm, and red box size is 10 × 10 μm.

Author Manuscript

Author Manuscript

Author Manuscript

Table 1.

Comparison of Visibility Values When Observing Nanostructures on a Blu-ray Disc[a]

	5×	10×	20×	50×
with PS-20	0.439	0.600	0.649	0.426
without PS-20	0.058	0.088	0.128	0.159

[a]As viewed through a PS-20 microparticle with different magnifications of the microscope objective. Comparative values of the objective lens without microparticles are also provided.